

Mercury's Atmosphere: A Surface-Bounded Exosphere

Deborah L. Domingue · Patrick L. Koehn · Rosemary M. Killen · Ann L. Sprague ·
Menelaos Sarantos · Andrew F. Cheng · Eric T. Bradley · William E. McClintock

Received: 28 August 2006 / Accepted: 7 August 2007 / Published online: 24 October 2007
© Springer Science+Business Media B.V. 2007

Abstract The existence of a surface-bounded exosphere about Mercury was discovered through the Mariner 10 airglow and occultation experiments. Most of what is currently known or understood about this very tenuous atmosphere, however, comes from ground-based telescopic observations. It is likely that only a subset of the exospheric constituents have been identified, but their variable abundance with location, time, and space weather events demonstrate that Mercury's exosphere is part of a complex system involving the planet's surface, magnetosphere, and the surrounding space environment (the solar wind and interplanetary magnetic field). This paper reviews the current hypotheses and supporting observations concerning the processes that form and support the exosphere. The outstanding questions and issues regarding Mercury's exosphere stem from our current lack of knowledge concerning the surface composition, the magnetic field behavior within the local space environment, and the character of the local space environment.

Keywords Atmospheres · Exosphere · Mercury · Space physics · Space weathering · MESSENGER

D.L. Domingue (✉) · A.F. Cheng
The Johns Hopkins University Applied Physics Laboratory, Laurel, MD 20723, USA
e-mail: deborah.domingue@jhuapl.edu

P.L. Koehn
Department of Physics and Astronomy, Eastern Michigan University, Ypsilanti, MI 48197, USA

R.M. Killen · M. Sarantos
University of Maryland, College Park, MD 20742, USA

A.L. Sprague
Lunar and Planetary Laboratory, University of Arizona, Tucson, AZ 86721, USA

E.T. Bradley · W.E. McClintock
Laboratory for Atmospheric and Space Physics, University of Colorado, Boulder, CO 80303, USA

1 Introduction

The discovery of an atmosphere, or more accurately an exosphere, around Mercury was made through the ultraviolet airglow and occultation experiments on the Mariner 10 spacecraft during its three flybys of the planet in 1974 and 1975. The Mariner 10 occultation experiment set an upper limit on Mercury's atmospheric density of approximately 10^5 atoms/cm³, corresponding to a pressure of about 10^{-12} bar (Broadfoot et al. 1976; Hunten et al. 1988), thus defining it as a collisionless exosphere with its exobase coincident with Mercury's surface: a surface-bounded exosphere. Ultraviolet (UV) emissions of the three atomic elements, hydrogen (H), helium (He), and oxygen (O), were detected with the UV airglow spectrometer (Broadfoot et al. 1976; Kumar 1976). Since the Mariner 10 flybys, exploration of Mercury's exosphere has been conducted by means of ground-based telescopic observations. Three additional elements, sodium (Na), potassium (K), and calcium (Ca), have been detected through their resonance scattering emission lines (Potter and Morgan 1985, 1986; Bida et al. 2000). Because the combined pressures of the known species are much less than the total exospheric pressure measured by the Mariner 10 occultation experiment, other species are expected to exist in this tenuous atmosphere. Additional constituents, such as carbon (C), carbon monoxide (CO), carbon dioxide (CO₂), lithium (Li), argon (Ar), neon (Ne), and xenon (Xe) have been sought but not detected (Broadfoot et al. 1976; Fink et al. 1974; Hunten et al. 1988; Sprague et al. 1996). Other species, such as hydroxyl (OH) and sulfur (S), have been suggested (Slade et al. 1992; Butler et al. 1993; Sprague et al. 1995) and modeled (Killen et al. 1997; Koehn 2002; Koehn et al. 2002) as related to the radar-bright deposits near Mercury's poles (Harmon and Slade 1992; Slade et al. 1992).

Telescopic observations from the mid-1980s to today have shown that there is temporal and spatial variability in Mercury's exosphere. The elements have both high- and low-velocity components and are influenced by the thermal and radiative environments in addition to the interstellar medium. For example, the variability in exospheric Na has been mapped to variability in the solar wind (Killen et al. 1999, 2004a, 2004b) and its effects on Mercury's magnetosphere.

Mariner 10 also made the first in situ measurements of the planet's magnetic field (Ness et al. 1974; Simpson et al. 1974) and the space environment around Mercury (Ogilvie et al. 1977). During the first flyby the spacecraft passed through the magnetotail of the planet and provided the first hint that Mercury may have a magnetic field similar to, though of lower amplitude than, the Earth's. The second flyby passed across the dayside of the planet, and the third again crossed the tail, this time closer to the planet's surface. Analysis of these data showed that the planetary magnetic field was probably a dipole with a moment of 350 to 400 nT-R_M³, oriented within 10° of the rotational axis (Connerney and Ness 1988). Additional details concerning Mercury's magnetosphere can be found in a companion paper (Slavin et al. 2007).

The fundamental observation, however, was that the magnetic field of Mercury is able to stand off the solar wind, at least under nominal solar wind conditions. This implies a dynamical coupling to the planet that is mediated by magnetospheric current systems that must close near or within the planet. At Earth, the corresponding current systems close in Earth's ionosphere, but Mercury has no ionosphere. How do the required current systems close at Mercury? One hypothesis is that Mercury's exosphere provides a so-called "pick-up conductance," derived from the ionization and electric field acceleration of atmospheric species, that enables the formation of an Earth-like magnetosphere despite the absence of an ionosphere (Cheng et al. 1987; Ip 1993). Another proposed mechanism for closing current systems is based on the assumption that the surface of Mercury is itself conducting

(Janhunen and Kallio 2004). As will be discussed, the exosphere, magnetosphere, and surface of Mercury form a complex, interacting system whose properties and dynamics are still incompletely understood.

Exosphere–surface interactions for many of the exospheric constituents are not well understood, since many properties of Mercury's regolith, such as porosity and composition, are still poorly known (Head et al. 2007; Boynton et al. 2007). Given the variability of solar wind conditions at Mercury's orbit, and the relative weakness of Mercury's magnetic field, the solar wind at times can drive the magnetopause down to the surface of the planet. Under these unusual conditions the surface is exposed directly to solar wind plasma and particles. Even under normal solar wind conditions, solar wind plasma and particles can access the magnetosphere and surface via a variety of processes, such as dayside reconnection creating open field lines or boundary layer processes. The composition of Mercury's exosphere, with its abundant H and He, clearly indicates a strong solar wind source. Once solar wind plasma and particles gain access to the magnetosphere, they predominantly precipitate to the surface, where solar wind species are neutralized, thermalized, and released again into the exosphere. Moreover, bombardment of the surface by solar wind particles, especially energetic ions, contributes to ejection of neutral species from the surface into the exosphere (via “sputtering”) as well as other chemical and physical surface modification processes. Details concerning the resulting “space weathering” of the regolith from scouring by solar wind particles are given by Head et al. (2007).

This paper summarizes our current state of knowledge concerning the exosphere composition, especially in terms of sources, sinks, and processes. It discusses the observed structure and density distributions within the exosphere and their association with the local environment. Exosphere–surface interactions and modeling efforts are compared with the current set of observations. The complex interaction and interconnections between the space environment (solar wind and interplanetary magnetic field, or IMF) and Mercury's magnetic field, exosphere, and surface are examined. Last, predictions are summarized for what the MErcury Surface, Space ENvironment, GEochemistry, and Ranging (MESSENGER) mission may observe and discover.

2 Composition: Sources, Sinks, and Processes

Table 1, adapted from Strom and Sprague (2003), summarizes the currently known constituents in Mercury's atmosphere and their approximate abundances. The abundance of H in Mercury's exosphere is at least 10 times the abundance seen in the Moon's exosphere

Table 1 Mercury's exospheric species

Constituent	Discovery reference	Column abundance (atoms per cm ²)
Hydrogen (H)	Broadfoot et al. (1976)	$\sim 5 \times 10^{10}$
Helium (He)	Broadfoot et al. (1976)	$\sim 2 \times 10^{13}$
Oxygen (O)	Broadfoot et al. (1976)	$\sim 7 \times 10^{12}$
Sodium (Na)	Potter and Morgan (1985)	$\sim 2 \times 10^{11}$
Potassium (K)	Potter and Morgan (1986)	$\sim 1 \times 10^9$
Calcium (Ca)	Bida et al. (2000)	$\sim 1 \times 10^7$

(Hunten and Sprague 1997). This large difference may be connected to the presence of a magnetic field on Mercury (Goldstein et al. 1981; Hunten and Sprague 1997). Goldstein et al. (1981) demonstrated that it is possible for Mercury's magnetosphere to stand off the normal solar wind (except at the high-latitude cusps). More recent hybrid models show that Mercury's magnetosphere is open a large part of the time (Kallio and Janhunen 2003a, 2003b, 2004a, 2004b). The distribution of Na atoms (discussed in the next section) is commensurate with these more open models. The abundances of Na and K have been observed to vary diurnally (Sprague 1992; Sprague et al. 1997; Hunten and Sprague 2002; Schleicher et al. 2004), with latitude (Potter and Morgan 1990, 1997; Sprague et al. 1997), and in association with surface features such as the Caloris basin and radar-bright spots (Sprague et al. 1990, 1998). Localized enhancements of Na have been observed with both imaging and spectroscopic techniques (Potter and Morgan 1990, 1997; Sprague et al. 1990, 1997; Hunten and Sprague 1997). More details on these variations are addressed in the next section, which describes the structure and density distribution of materials within the exosphere.

Measurements of many of the exospheric constituents show evidence for two-component velocity (temperature) distributions (e.g., H), or for Weibull (a continuous probability distribution function) distributions (Na and K). The vertical distribution of H is best modeled by two components: a dominant cold component with a temperature characteristic of the cold nightside surface and a smaller component with a temperature distribution more commensurate with the hot dayside surface temperature (Shemansky and Broadfoot 1977; Hunten and Sprague 1997). Observations of Na indicate that this species is emitted into the exosphere at higher velocities (commensurate with sputtering from the surface by charged particles or energetic solar photons) and that thermalization to the surface temperature is inefficient (Hunten et al. 1988; Hunten and Sprague 1997; Killen et al. 1999). Models of the exosphere sources and sinks are constrained by the measurements of these multiple velocity or temperature components.

Table 2 outlines the possible sources, sinks, and processes producing Mercury's exosphere. The sources and sinks are related to a complex interplay between exosphere-surface interactions (discussed in more detail in Sect. 4) and solar wind, IMF, and planetary magnetospheric interactions (discussed in more detail in Sect. 5) with the surface.

The observed abundances of H and He can be explained by solar wind capture and radiogenic decay (^4He). These species are lost from Mercury's exosphere through thermal escape. Heavier atoms, such as Na and K, are lost by photoionization. Once ionized, roughly half are carried away by the solar wind (Killen et al. 2004a; Killen and Crider 2004). Most of those recycled return on the dayside depending on the scale height (Sarantos 2005). However, there is a small population of these ions that could be trapped in Mercury's magnetotail, accelerated back to the nightside of the planet, and recycled through interactions with the surface (Ip 1993; Hunten and Sprague 1997; Sarantos 2005).

The most extensively studied species in Mercury's exosphere is Na. Sodium has been observed to be highly variable, with column densities varying on timescales smaller than 24 hours. Distributions and enhancements of Na in the exosphere have been correlated with solar wind magnetospheric interactions and variations in the regolith composition (e.g., Potter and Morgan 1990, 1997; Killen et al. 1990, 1999, 2001; Sprague et al. 1997, 1998; Potter et al. 1999; Lammer et al. 2003). Killen et al. (2001) examined how much of the Na population could be attributed to photon-stimulated desorption (PSD), ion sputtering, and impact vaporization of micrometeoroids. They concluded that the impact vaporization process could provide up to 25% of the Na seen. The relative importance of each process is variable, both

Table 2 Mercury exosphere sources and sinks

Source processes	Relevant species	Recycling process	References
<i>Direct to exosphere</i>			
Solar wind capture	H, He		a, f
Radiogenic decay and outgassing	He		a, f
Meteoroid volatilization	Na, K, Ca		b, d, f, g
<i>Delivery to surface</i>			
Diffusion	H, He, O, Na, K		d, e, h, j, k, l, m
Regolith turnover	H, He, O, Na, K, Ca		d, e, f
Magnetotail or ion recycling	H, He, O, Na, K, Ca		a, c, e, k
<i>Release from surface</i>			
Sputtering: physical	Na, K, Ca	Yes	c, d, e, f, j
Sputtering: chemical	Na, K, Ca, OH	Yes	l, o
Thermal desorption (evaporation)	H, He, O, Na, K	Yes	d, f, k, l
Photon stimulated desorption (PSD)	Na, K	Yes	d, l
Impact vaporization	All		n
<i>Sink processes</i>			
Photoionization	H, He, O, Na, K, Ca		e, f, d, k
Thermal escape	H, He		f
Surface implantation: adsorption	H, He, O, Na, K, Ca	Yes	e, f, k
Surface implantation: chemical bonding	H, O, Na, K, Ca	Yes	f, m

a. Goldstein et al. (1981). b. Potter and Morgan (1985). c. Ip (1986). d. McGrath et al. (1986). e. Cheng et al. (1987). f. Hunten et al. (1988). g. Morgan et al. (1988). h. Tyler et al. (1988). i. Killen (1989). j. Sprague (1990). k. Sprague (1992). l. Hunten and Sprague (1997). m. Potter (1995). n. Cintala (1992). o. Potter (1995)

with true anomaly angle and with solar activity, and is highly uncertain. The remainder of the Na in Mercury's exosphere is considered to come from a combination of processes that deliver Na to the surface followed by a set of surface release processes.

The three processes listed in Table 2 that are believed to deliver exospheric material to the surface are diffusion, regolith turnover, and ion recycling. Diffusion processes can be subdivided into three types: regolith diffusion, volume diffusion, and grain-boundary diffusion. Regolith diffusion, as examined by Sprague (1990), is the diffusion of sodium

and/or potassium along cracks and voids between grains and rock fragments. Volume diffusion, as studied by Killen (1989), is the solid-state diffusion through crystalline lattices. Grain-boundary diffusion is the diffusion of material across grain surfaces. Killen (1989) found that volume diffusion is too slow to produce the Na abundance observed in Mercury's exosphere. Sprague (1990) suggested that the combination of regolith and grain-boundary diffusion can provide the requisite amounts of Na and K over the solar system lifetime without relying on efficient recycling of material. These diffusion processes can also explain the relative observed abundances of Na and K at the Moon (Sprague 1990). Mercury's highly variable Na/K abundance ratio, which is also much higher than the Na/K ratio observed for the Moon, remains unexplained (Potter et al. 2002a). However, potassium column densities have been observed to decrease with increasing levels of solar activity (Potter et al. 2002a), which led Ip and Kopp (2004) to postulate that the Na/K ratio variability, and high value compared with lunar values, may be caused by the favored removal of K through its preferential acceleration (resulting from its lower gyrofrequency compared with Na) by ion cyclotron waves generated in the polar caps due to solar wind interactions. However, Sarantos (2005) tested the hypothesis that there exist more fractional losses for potassium ions and found no statistical difference for the fractional recycling of Na^+ and K^+ due to acceleration by the large-scale electric field. A more likely explanation for the variable Na/K ratio is thermal diffusion acting faster on bound sodium than on potassium (Sprague 1992; Killen et al. 2004a). It is also quite possible that the observed variation in the Na/K ratio results from the fact that the two species were not observed concurrently and that spatial and temporal variations are the cause of the differences.

Regolith turnover is another mechanism for bringing exospheric material to the surface, namely through impact gardening. Ion recycling has been studied by Killen et al. (2004a), Killen and Crider (2004), and Sarantos (2005). Work by Ip (1993) showed that exospheric material, after ionization by solar UV photons, could be trapped in Mercury's magnetotail and transported to the nightside. Sprague (1992) suggested that these ions could be implanted into the nightside surface, where they can be neutralized and adsorbed into the surface. However, Sarantos' (2005) modeling shows that approximately twice as many ions recycle to the dayside, but this result is highly variable with IMF conditions. Dayside recycled photoions can be reemitted at short timescales due to PSD, but nightside recycled ions can be reemitted only by meteoritic vaporization, ion sputtering, and electron-impact sputtering. The emission rate on the nightside is probably one-third to one-half the dayside rate, depending on the impact vaporization rate and nightside sputtering rate.

Although meteoroid volatilization is listed in Table 2 as a "direct to exosphere" source process, volatiles released during the impact process may also be trapped within the surface for later release to the exosphere. Conversely, the impact process could also release exospheric species already present in the surface.

Once these materials are brought to the surface, a process is needed to release them to the exosphere. The release processes listed in Table 2 include sputtering (both physical and chemical), evaporation, meteoritic vaporization, and PSD. Physical sputtering is the release of material through impact by energetic particles. Chemical sputtering involves a chemical reaction between the surface material and the energetic particle, where the reaction product is desorbed. Chemical sputtering has been suggested as a source of Na and OH (Potter 1995). The high-velocity component observed in the Na emission lines indicates a high-energy mechanism for release of materials from the surface. This mechanism is commensurate with sputtering by either charged particles from the solar wind or solar photons. Thermal desorption, or evaporation, as proposed by McGrath et al. (1986), is too rapid to characterize the atmosphere alone, but it is part of the exosphere recycling process. PSD is the desorption

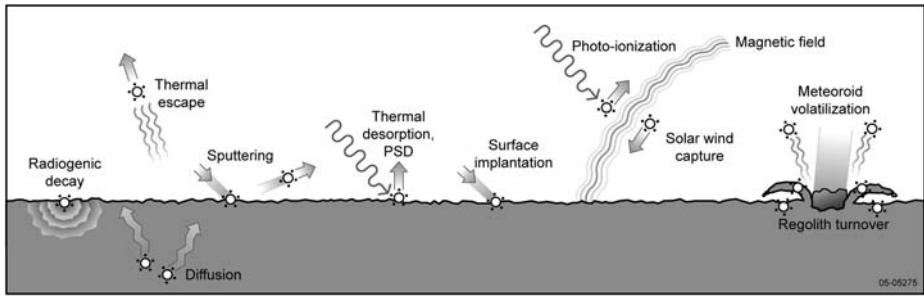


Fig. 1 The sources, sinks, and processes within the exosphere, surface, and magnetopause of Mercury

of particles due to UV photon bombardment. Laboratory studies by Yakshinskiy and Madey (1999) demonstrated that Na can be released via PSD from lunar soil simulate. Killen et al. (2001) modeled particle release from Mercury's surface by PSD and found that PSD could be an efficient particle release process on the dayside for volatile species such as Na and K. The strong observed dependence of Na abundance with solar zenith angle supports PSD as a major source process for Na (Killen et al. 2001). Refractory elements such as Ca would not be thermally desorbed or sputtered by UV photons. Refractory species are most efficiently released by impact vaporization (e.g., Mangano et al. 2007). Very hot calcium has been observed in the exosphere, a large fraction of which directly escapes (Killen et al. 2005).

The possible sinks for depleting Mercury's exosphere include thermal escape (H and He only), photoionization and entrainment in the solar wind, and surface implantation. Neutral atoms in the exosphere can be ionized and removed to the interplanetary medium via the solar wind and magnetosphere (Killen et al. 2004a; Killen and Crider 2004; Sarantos 2005). Thermal escape is an efficient process for the lighter elements H and He. Thermal escape assisted by solar radiation pressure occurs for sodium and presumably also for potassium. Up to 10% of the total sodium production rate is lost by escape into the Mercury "tail" during periods of maximum solar radiation pressure (Potter et al. 2002b). Removal of material from the exosphere via surface implantation can occur either through adsorption onto surface grains or through chemical interactions, such as those that produce space weathering effects in the regolith. Adsorption is more productive on the nightside, where evaporation is less effective at releasing the material. Adsorption also includes the process of cold-trapping material, such as in shadowed areas at high latitudes, or under outcroppings (Yan et al. 2006). The accumulation of material on the nightside for later release during Mercury's day is supported by the diurnal variations seen in the Na abundances (Sprague 1992; Sprague et al. 1997; Hunten and Sprague 2002; Schleicher et al. 2004).

The life cycle (Fig. 1) of an exospheric species can be followed by starting its journey to the surface from either the subsurface (by diffusion or regolith turnover) or from the exosphere (by collision with the surface) (Killen and Crider 2004). If a neutral atom collides with the surface it can be either scattered back into the exosphere or implanted into the surface, where it is either adsorbed or chemically bonded in a surface space-weathering process. A photoionized species can also collide with the surface (Killen et al. 2004a; Sarantos 2005), where it will be either neutralized and adsorbed (such as with magnetotail or ion recycling) or chemically bonded into the surface, also as part of the space-weathering process. Species from the surface can be introduced, or reintroduced, into the exosphere by sputtering, evaporation, PSD, meteoroid volatilization, impact vaporization, or scattering from collision at the surface.

3 Structure and Density Distributions

Several sets of observations constrain the six known constituents (H, He, O, Na, K, and Ca). Atomic hydrogen, observed in two height distributions, is characterized by the day and night surface temperatures, respectively, with scale heights above the surface of about 1,330 and 230 km. Helium emission, greatest over the dayside and above the sunward limb, was measured as far as 3,000 km above the surface (Broadfoot et al. 1976). The Mariner 10 observations did not include measurements in the polar regions, so the distribution associated with those areas is constrained only by telescopic measurements. Telescopic observations show that Ca appears to be enhanced above the polar regions, but its distribution is not fully known (Killen et al. 2005). Calcium is observed at extreme temperatures, and a large fraction is above escape velocity (Killen et al. 2005). The mechanism for imparting these energies is unknown. For O, observations by Mariner 10 provided only an upper limit on the abundance estimate.

Ground-based observations of Na and K show variable abundances and distributions of these elements. Possible associations between bright-ray craters and regions of freshly overturned regolith with enhanced Na abundance, as indicated by emission at the Na D2 line at 589 nm (Sprague et al. 1998), are shown in Fig. 2. The brightest Na emission falls over the Kuiper-Muraski crater complex (designated K) and the location of features with notably bright albedo at both visible and radar wavelengths (A). Both of these geologic features are associated with regions of freshly excavated material (Robinson and Lucey 1997; Harmon 1997). The brightest region in the figure appears offset from the associated geologic features. Atmosphere turbulence effects, or atmospheric seeing, would move the bright region toward the center of the image; thus it is more likely associated with the features closer

Fig. 2 This Na emission image, adapted from Potter and Morgan (1997), was taken with an image slicer on the McMath-Pierce Solar Telescope at Kitt Peak. It shows an example of enhanced Na emission observed over a freshly cratered region (K, Kuiper-Muraski crater complex). A radar-bright spot (A) is at the longitude of the limb. Both areas K and A are associated with regions of freshly overturned regolith. Radar-bright spot B is at the same longitude in the northern hemisphere but shows no enhancement of Na. Localized Na sources near the planet limb observed from ground-based telescopes appear offset in the direction of the planet center due to atmospheric seeing effects. Thus the bright red region is likely associated with geologic features near the limb. The color bar codes the intensity of emission, with red the brightest (~ 6 MRayleighs for the date of observation; December 7, 1990) and blue-green the minimum

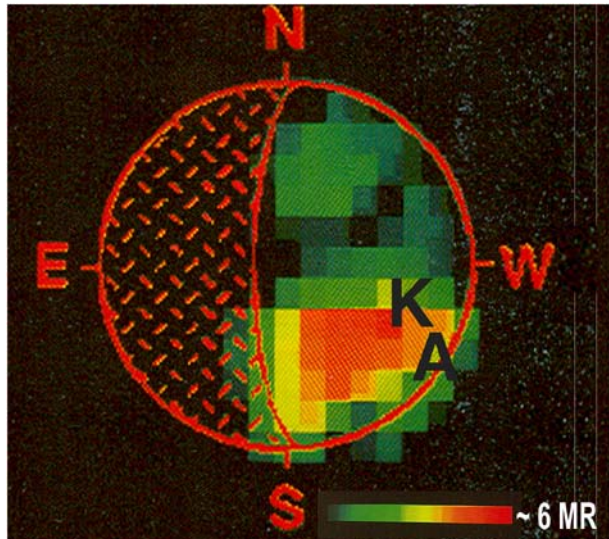
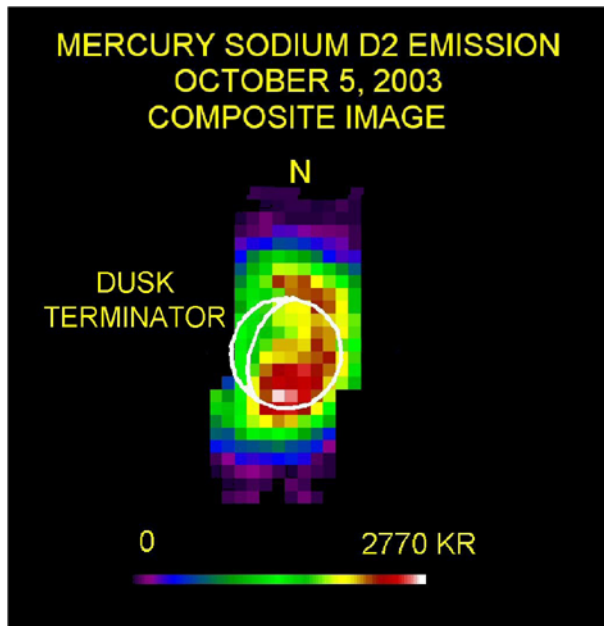


Fig. 3 An example of the asymmetric distribution of Na in Mercury's atmosphere (Potter et al. 2006). This observation, made near Mercury's perihelion, is a composite of three $10'' \times 10''$ images taken with the image slicer on the echelle spectrograph at Kitt Peak's McMath-Pierce Solar Telescope. Each pixel is $1''$ square and is produced by extracting the D2 emission line from a high-resolution spectrum. The figure shows integrated intensity along the line of sight in kRayleighs (kR) and is not in a 1 : 1 relationship to zenith column abundance. The tail is not imaged here since only three $10'' \times 10''$ fields are shown. Limb brightening is apparent on the dayside due to line of sight effects

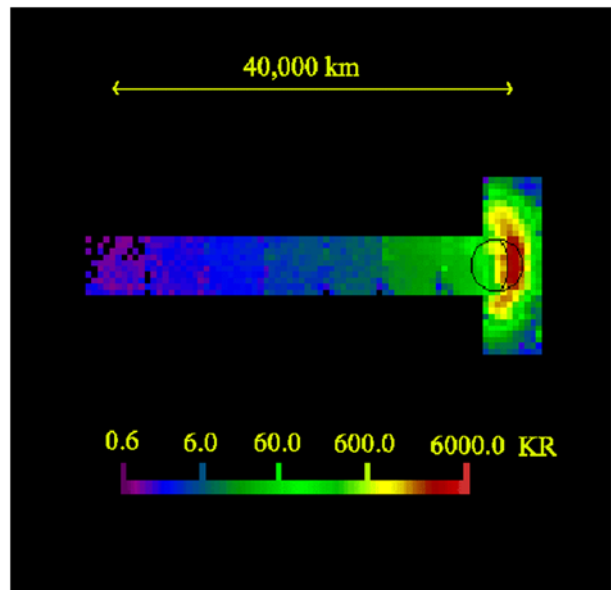


to the limb. In addition, the processing of image data obtained from an image slicer to a representative two-dimensional map also shifts the location of the bright region. With this said, it should be noted that the distribution of these elements changes on a daily basis and this distribution could be a function of magnetosphere–solar wind interactions (Killen et al. 2001). Another example of the uneven distribution of atmospheric sodium (Fig. 3) is the observation of brightening along the sunlit limb and excess sodium at high southern latitudes (Potter et al. 2006). In this case peak emission is observed at ~ 2.7 MRayleighs (2,700 kR).

Sodium and potassium atoms are massive enough to be mostly bound to the planet, and thermal components with scale heights roughly approximated by the surface temperature (30–60 km) are present (Sprague et al. 1997). However, several ground-based observations have found an extended Na component that varies in distance according to Mercury's true anomaly, solar activity, and the orientation of magnetic fields in the solar wind (Potter et al. 2006). Scale heights of 150 km have been used to model the observed Na distributions seen by Schleicher et al. (2004). Figure 4, adapted from Potter et al. (2002) and obtained from Kitt Peak's McMath-Pierce Solar Telescope, shows three regimes of the Na exosphere. Extended coronae sometimes exist above both the north and south polar regions; a lower-scale height region can be observed at the subsolar point; and there is a "tail" of material streaming in the anti-sunward side. All of these three regimes are expected as a result of solar radiation pressure. The abundance of the distant tail population is controlled by pressure from solar photons and various source mechanisms. Thus the tail's extent is expected to vary with the position of Mercury relative to the Sun and has been modeled by Smyth and Marconi (1995) and Leblanc and Johnson (2003).

Figures 5 and 6 show two extreme examples taken from the models of Leblanc and Johnson (2003). The exosphere model simulation by Leblanc and Johnson (2003) includes a surface source of atoms from an initially adsorbed layer of 4×10^{12} atoms cm^{-2} as well as what is provided by infalling meteoritic material. As discussed in Sect. 4, these researchers do not consider such other sources as diffusion and meteoritic vaporization. In their model

Fig. 4 Emission from Na atoms in Mercury's exosphere and anti-sunward tail are shown along with a *color bar* indicating emission intensity in kRayleighs (Potter et al. 2002b). This image was taken on May 26, 2001, at a Mercury true anomaly of 130° . This is a composite of ten $10'' \times 10''$ images taken with an image slicer on the echelle spectrograph at the McMath Pierce Solar Telescope. Resonance scattering reveals sodium only in sunlight; therefore, the relatively low emission to the left, on the nightside, does not mean that there is a lack of sodium there. The Na distribution and emission intensity are variable and depend on true anomaly as well as variable source processes. Line-of-sight velocity was determined by measuring the shift of the centroid position of the emission line from the rest position on Mercury. These velocities were converted to heliocentric velocities by dividing by the sine of the phase angle. This image, made close to aphelion, shows the Na extended high above the polar regions similar to the model shown in Fig. 5



atoms accumulate on the nightside, and as a consequence the morning terminator is the main source of sodium atoms to the atmosphere. Leblanc and Johnson (2003) concluded that the north–south asymmetries can be attributed to maxima in surface Na concentration at high latitudes just before the dawn terminator due to cold trapping.

Alternative models (as discussed in Sect. 4), such as that proposed by Killen et al. (2001, 2004a), incorporate additional processes. In these models cold-trapping is less efficient on the nightside because impact vaporization and ion sputtering deplete the surface of adsorbed atoms, and because many of the atoms that reach the nightside are already above escape velocity. As a result, the exosphere is most dense on the dayside, either at the subsolar point or with local enhancements where the magnetosphere is open to the solar wind.

Measurements of the distribution and abundance of the Na atmosphere above the limb of Mercury were made during Mercury's transit of the Sun in 2003 (Schleicher et al. 2004). Using a triple etalon system with adaptive optics, the absorption profile of the Mercury Na D2 line was measured. Na emission was observed to be greater above both polar regions than above the equatorial limb of the planet. In addition, measurements above the morning side of the planet exhibited greater Na emission than on the evening side. The predictive model of Leblanc and Johnson (2003) shown in Fig. 5 is consistent with the observations, which also occurred near aphelion. Schleicher et al. (2004) give Na scale heights for four geometries

Fig. 5 At aphelion, at a true anomaly angle of 181° , the Na exosphere is extended above the polar regions on the Sun side in this model (Leblanc and Johnson 2003). The abundance units on the color bar are logarithmic in Na/cm^2 and distances are in units of planet radius

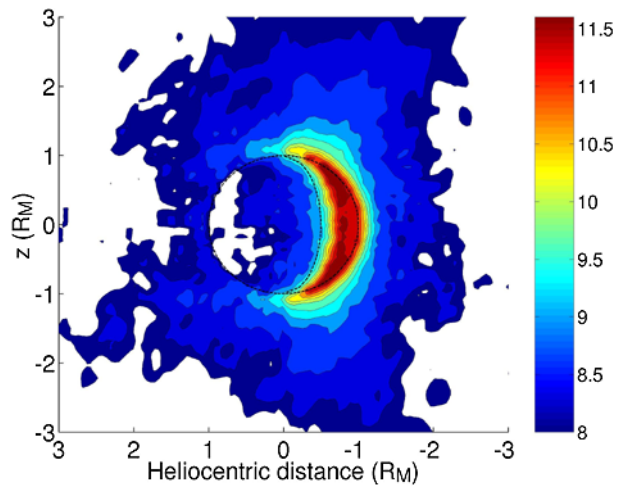


Fig. 6 At a true anomaly of 252° the maximum Na emission appears near the morning terminator in this model from Leblanc and Johnson (2003). As described in the text, the Na streams behind the planet under the increased influence of solar radiation pressure. This geometric configuration corresponds closely to that shown in Fig. 4. Column abundance units on the color bar are logarithmic in Na/cm^2

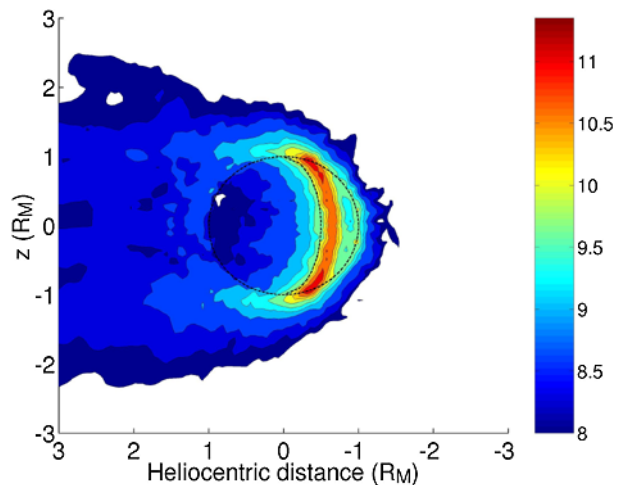


Table 3 Estimate of sodium scale heights

Location	Scale height (km)
Northern maximum	135 ± 30
Southern maximum	130 ± 30
Western planetary limb	(150)
Eastern planetary limb	(150)

at Mercury's limb, corresponding to the equivalent widths shown in Fig. 7. Good model fits to the northern and southern maximum measurements give scale heights with error bars as shown in Table 3. For the eastern and western planetary limbs, a scale height of 150 km was assumed for the model (shown in parentheses). Note that equivalent atmospheric temperatures corresponding to these scale heights are between 1,350 and 1,520 K, consistent with the results of Na D2 line width modeling by Killen et al. (1999).

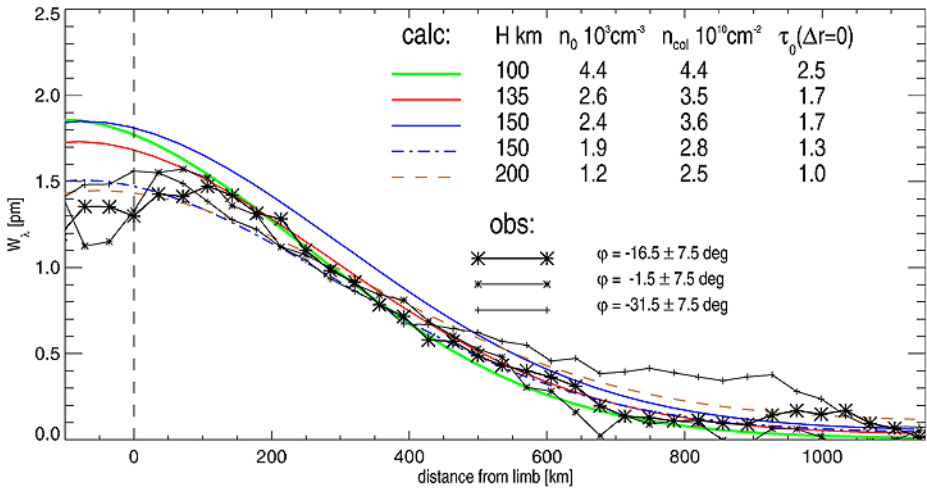


Fig. 7 Equivalent widths of the Mercury Na D2 line are plotted as functions of the distance from Mercury's limb. Models estimating fits to the equivalent width distributions yield estimates of the scale height (H) of the Na distribution (Schleicher et al. 2004). φ is the azimuthal angle from the north pole of Mercury measured in a clockwise direction around the observed limb of the Earth-facing disk, τ_0 is the optical depth at the line's center along the gazing line of sight, n_0 is the Na particle density, and n_{col} is the Na column density

An estimate of about 1.6 km s^{-1} is made for the velocity along the line-of-sight of the measurement. This estimate is based on the Doppler width of the Na D2 line convolved with the spectral resolution of the instrument.

Some information regarding the height distribution of Ca above Mercury's surface has been obtained by several spectroscopic measurements (Killen et al. 2005). Figure 8a shows intensity of Ca 422.6 nm emission at the slit locations during one such observing period, with the Ca intensity color coded. Figure 8b shows the corresponding line of sight Ca velocity corresponding to the slit locations shown in Fig. 8a. Clearly a high-energy process is placing Ca up to 3,000 km above Mercury's surface. No near-surface Ca emission has yet been found on the sunlit limb due to the difficulty of observing near the bright limb. The data shown in Fig. 8 indicates that Ca is moving at extreme velocity in the direction of orbital motion of Mercury, with a large fraction probably moving above escape velocity. These velocities cannot be due to impact vaporization or ion sputtering but must be caused by a secondary process such as dissociation or charge exchange (Killen et al. 2005).

No actual measured information regarding the height distribution of O is available (the detection and estimated abundance of O made by Mariner 10 had no associated height distribution information, and ground-based observations cannot detect the emission line at 130.4 nm because of telluric atmospheric opacity in the UV). It is possible that Ca may be vaporized in molecular form, and that CaO is dissociated after ejection from the surface, leaving both Ca and O at high energy (Killen et al. 2005). In such a case it could be expected that O will be escaping. Koehn and Sprague (2007) suggested that O^{6+} and Ca^{11+} delivered by the solar wind to Mercury's surface and subsequently ejected as neutral atoms into an energetic distribution in the Mercury space environment or exosphere are adequate to explain the observations.

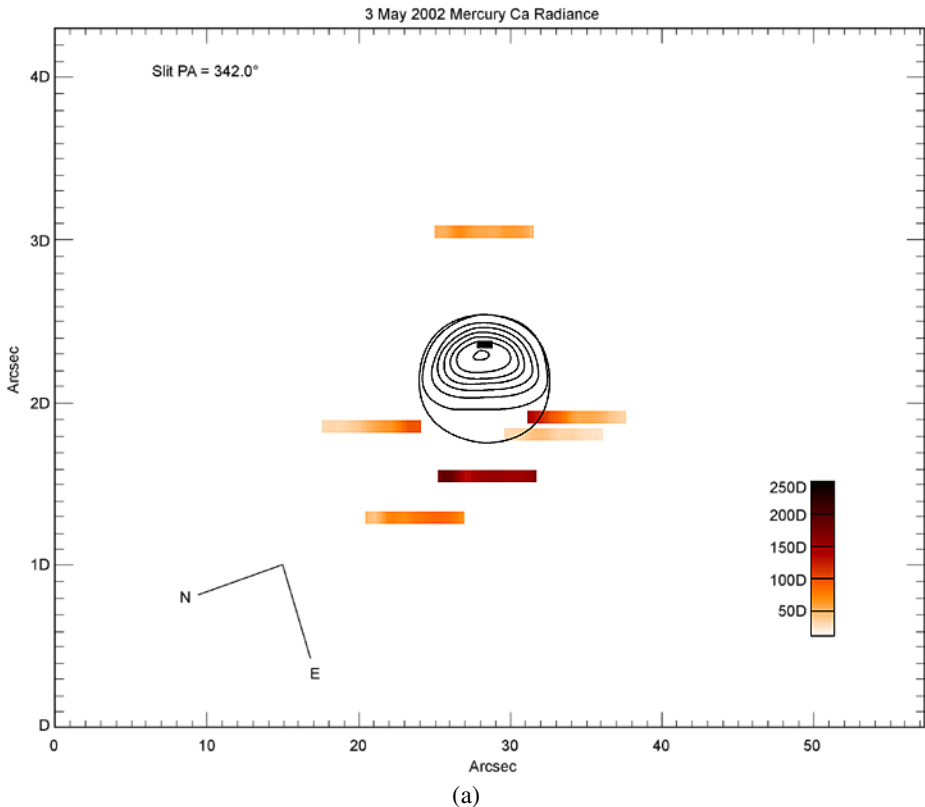


Fig. 8 (a) Intensity of Ca emission at various slit locations of the High Resolution Echelle Spectrometer (HIRES) placed from the limb to about one Mercury diameter away from the planet during observations at the Keck I telescope on May 3, 2002. (b) Line-of-sight velocity components of calcium of 1 to 3 km/s are color coded, corresponding to the slit locations in (a). They indicate extreme velocity in the direction of orbital motion of the planet, probably on the order of 1.5 to 4. km/s. A large fraction of the calcium is probably above escape velocity

4 Exosphere–Surface Boundary Interactions

Early theoretical treatments of Mercury's (and the Moon's) tenuous atmosphere assumed the surface was saturated with an adsorbate (e.g., Hodges 1973; Hartle and Thomas 1974; Hartle et al. 1973). This assumption defined a process in which every impact of an atom is followed by the release of another similar atom at the impact site. Hartle and Thomas (1974) assumed that the source of the lunar atmosphere is the solar wind, and that the flux of solar wind particles hitting the surface is balanced by the rising flux. Therefore an equilibrium is assumed between incoming solar wind ions and outgoing neutrals. A similar model was derived for Mercury (Hartle et al. 1973), but it was invalidated by Mariner 10's discovery of an intrinsic magnetic field.

Classical exospheric models, derived for an exosphere whose exobase is in contact with an atmosphere, are based on the assumption that the exospheric constituents are derived from a reservoir of atoms whose source is freely evaporating with a Maxwellian velocity distribution equivalent to the local surface temperature. The resulting altitude distributions follow a barometric law with certain deviations due to loss by escape (Chamberlain 1963). How-

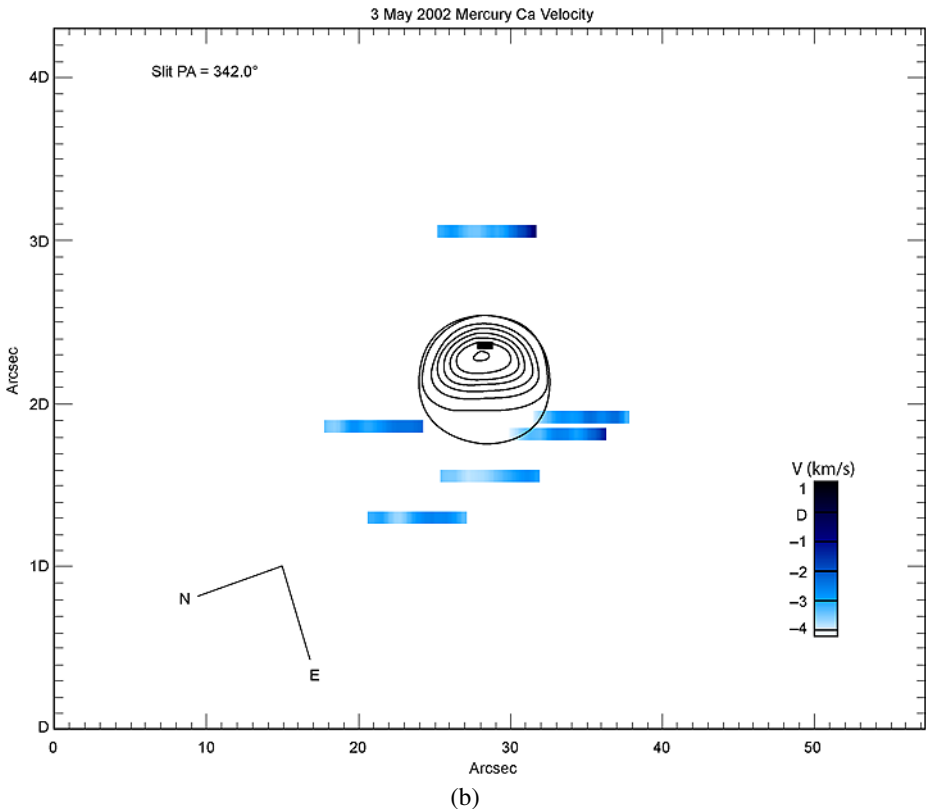


Fig. 8 (Continued)

ever, it is evident that many details of these models are not consistent with surface-bounded exospheres. For a surface-bounded exosphere, the expected source processes include PSD, ion sputtering, and meteoritic vaporization (see Table 2). The first two processes produce a source whose velocity distribution is described by a statistical Weibull distribution at an equivalent temperature of about 1,200 K (Madey et al. 1998). Unlike a Maxwellian velocity distribution, this distribution is much hotter than the surface and includes a tail distribution of very hot atoms. Vapor derived from meteoritic vaporization produces a gas that is thermal, but very hot, about 3,000 to 5,000 K (Kadono and Fujiwara 1996; Kadono et al. 2002; Sugita et al. 2003). Therefore classical exospheric models are not directly applicable to Mercury's exosphere.

The degree to which atoms thermally accommodate to the surface on contact is not well known and is probably species dependent. The global distribution of H and He in Mercury's exosphere as measured by Mariner 10 is incompatible with thermal accommodation. Models based on the assumption of thermal accommodation predict an anti-solar/subsolar He number density ratio of 200 at the surface. However, the measured ratio is smaller, by a factor of about 10. Altitude distributions of the known gases in Mercury's exosphere, when fit to a scale height, give temperatures that are different for each constituent. The H seen above the subsolar point has both a very cold component and a warm component, which at 420 K is colder than the surface at that location. Helium was fit to a 575 K barometric atmosphere above the subsolar point, which is closer to the subsolar temperature. However,

the anti-solar density observed for He is much less than that predicted on the basis of thermal accommodation. Sodium line profiles measured near the surface (not in the tail, which is accelerated by radiation pressure) are consistent with a much hotter gas than the surface. The Na exosphere is measured to be 1,200 K at the equator and 750 K at the poles, or at least 550 K hotter than the surface (Killen et al. 1999). The original Na D2 line width measured by Potter and Morgan (1985) was shown to be consistent with $\sim 90\%$ of the Na atoms at 500 K and the remaining $\sim 10\%$ at even higher temperatures (Hunten et al. 1988), suggesting that different locations and times of measurement have different equivalent temperature distributions. The only other known constituent of Mercury's atmosphere, Ca, has been observed and modeled with temperatures consistent with a very hot gas (6,000 to 12,000 K) (Bida et al. 2000). These temperatures indicate that nonthermal processes are important in producing and maintaining Mercury's surface-bounded exosphere, and that none of the known constituents is in thermal equilibrium with the surface.

Another variable in the exosphere–surface boundary models is the sticking time, or the time between impact of the downwelling atom and its rerelease into the atmosphere. Long sticking times imply chemisorption (absorption resulting in a chemical bond) or physisorption (absorption into an atomic potential well resulting in a physical bond). It has been suggested that atoms that stick to the surface become bound and do not have lower binding energies than atoms intrinsic to the rock (Madey et al. 1998). The binding energy of sodium is somewhat controversial, but there may be a variety of binding sites on a silicate surface, particularly for a radiation-damaged surface (Yakshinskiy et al. 2000). In addition, the sticking efficiency on a porous surface such as a regolith is greater than the sticking efficiency on a flat surface due to multiple interactions with the surface on each impact. On silicate surfaces, the sticking efficiency is about 0.5 at $T_s = 250$ K and decreases to a value of 0.2 at $T_s = 500$ K (Johnson 2002).

While Johnson (2002) argued that most collisions with the surface are free-bound (the atom is adsorbed or goes through a bound state prior to scattering), Shemansky and Broadfoot (1977) argued that the surface of Mercury is not saturated with gas and that most collisions of light atoms with the planetary surface are “free–free” (the atom is unbound before and after the collision and does not go through a bound state), not free-bound. Measured energy accommodation coefficients for He and Ne are quite small (0.009–0.07 and 0.06–0.3, respectively), while accommodation coefficients for Ar can be large (0.29–0.67). Shemansky and Broadfoot (1977) argued that collisions that do not involve adsorption are limited in the amount of energy that can be gained or lost to the substrate at each collision. This situation is consistent with a gas that is derived from an energetic process such as ion sputtering or meteoritic vaporization and remains hotter than the surface. It also explains the uniformity of the H atmosphere relative to that predicted on the basis of thermal accommodation.

Thermal vaporization rates are critical to the resulting source rates and velocity distributions of the constituents in Mercury's exosphere. The role of thermal vaporization rates is especially controversial in how they are treated in various exosphere–surface interaction models. Thermal vaporization rates are governed by the binding energy of the atom balanced against the temperature. The more tightly bound the atom, the lower the thermal vaporization rate, but the higher the temperature, the higher the vaporization rate. The controversy over the effect of thermal vaporization on the surface of Mercury arises from the recognition that vaporization at equatorial latitudes near the subsolar region will deplete a monolayer of sodium atoms quite quickly. Some models, such as that of Leblanc and Johnson (2003), do not include any additional source of atoms at the exobase, e.g., through meteoritic vaporization or diffusion (including regolith, volume, and grain-boundary diffusion). Given these assumptions, a rapid depletion of sodium at equatorial latitudes on the sunlit side of Mercury

will occur. Leblanc and Johnson (2003) concluded that the hot equatorial surface becomes depleted in adsorbed sodium, thus shutting down the supply of atoms to the exosphere.

Sprague (1990) and Killen et al. (2004a) showed through modeling that the source of Na atoms through grain-boundary diffusion and meteoritic vaporization taps a deeper source and is therefore not depleted through thermal vaporization. Killen et al. (2004a) concluded that a source of atoms to the extreme surface from the grains is robust enough to maintain PSD, ion sputter, and meteoritic vapor rates, and therefore these source rates for these processes are independent of the abundance of adsorbed atoms. In other words, thermal vaporization taps a different reservoir of atoms than the other three source processes.

Killen et al. (2004a) also showed that regolith gardening is fast enough on Mercury to replenish the supply of sodium to the surface for the age of Mercury. Regolith gardening rates are known for the Moon (Heiken et al. 1991). Killen et al. (2004a) assumed that the regolith gardening rate can be scaled linearly to the meteoroid influx, which they assume is roughly an order of magnitude larger at Mercury than that at the Moon. The scaled micrometeoroid flux is based on measurements at Earth orbit (Cintala 1992), and the flux of larger meteoroids estimated from Spacewatch measurements (Marchi et al. 2005). These results, however, are quite uncertain and will not be fully characterized without in situ measurements. Meteoroid impacts supply the surface with fresh rock from below and bury the top layers of regolith.

In addition to regolith gardening, meteoroid and micrometeoroid impacts affect the composition and storage of volatiles through vapor deposition. Although some of the vapor derived from meteoroid impact is lost to the system, much of it is retained (Butler et al. 1993; Crider and Killen 2005). The regolith grains at Mercury are most likely coated with glass derived from impact vapor. Since glass is amorphous, atoms more readily diffuse through it and evaporate from it (Shih et al. 1987). Thus source rates for the atmosphere from the surface-boundary exobase are intimately dependent on meteoroid impact rates and on the distribution of the impact vapor.

In modeling exosphere–surface boundary interactions, another effect that should be considered is the impact of surface charging on sputtering. Surface charging has been shown to be an important process at both Mercury (Grard 1997) and the Moon (Vondrak et al. 2004) due to efficient photoionization and interaction of the surface with solar wind ions and possibly with ions of planetary origin. Surface charging affects the trajectories of photoions (Grard 1997) and hence recycling rates for photoions (Killen et al. 2004b). There is a possibility that charged dust levitates on Mercury as well as on the Moon (Stubbs et al. 2005). Surface charging also will affect the rates and energies of ion sputtering since about 10% of the sputter products will be ions (Elphic et al. 1993). For example, low-energy electrons can cause negative charging and enhance outward diffusion of sodium (Madey et al. 2002).

The rates and effectiveness of ion sputtering as a process for producing and maintaining Mercury's exosphere are strongly affected by the local space environment. Mercury's surface is shielded from the solar wind by its magnetosphere to an extent dependent on the solar wind dynamic pressure and on the magnitude and direction of the IMF. This magnetosphere is a dynamic system that can vary dramatically between being closed or open (Kabin et al. 2000; Sarantos et al. 2001; Kallio and Janhunen 2003a, 2004a, 2004b). The solar wind can impinge on a large fraction of the dayside surface when the magnetosphere is in its open configuration. The effect of the solar wind impinging on the surface is controversial, and much is based on studies of the lunar exosphere, some of which is contradictory. While early models were based on the assumption that the lunar surface simply acts as a sponge for solar wind particles (Hartle and Thomas 1974), the rapid variation in the observed sodium atmosphere of Mercury prompted some observers to postulate that the heavy ions in the solar wind or interplanetary medium are quite effective in

sputtering atoms, particularly sodium atoms, from the surface (Potter and Morgan 1990; Potter et al. 1999; Killen et al. 2001). Recent work has shown that highly charged heavy ions can be orders of magnitude more effective at sputtering insulator targets than singly charged ions of the same species (Shemansky 2003; Aumayr and Winter 2004). Thus heavy ions in the solar wind can be as effective or even more effective at sputtering than the more abundant H^+ and He^{++} in the solar wind. The resulting atmosphere would be asymmetric, as is observed, since the magnetosphere is expected to be asymmetric north/south due to the sunward component of the IMF (Sarantos et al. 2001; Leblanc and Johnson 2003). In addition to directly sputtering atoms from the surface, the solar wind ions hitting the surface can produce radiation damage, which enhances the efficiency of PSD (Potter et al. 2000). The role of magnetospheric shielding and its effects on the ion-sputtered production of Na can be tested by observations of the lunar atmosphere as the Moon moves inside and outside of the Earth's magnetosphere. Potter et al. (2000) showed evidence in lunar atmospheric Na observations that even though the Moon is fully in sunlight, its atmospheric density begins to decline as soon as it enters the Earth's magnetosphere, where it is shielded from the solar wind and continues to decline until the Moon reemerges from the magnetosphere. However, lunar corona observations by Mendillo and Baumgardner (1995) and Mendillo et al. (1999) of the Moon during eclipse show consistent atmospheric Na abundances regardless of the Moon's position within the Earth's magnetosphere. From an analysis of these observations Mendillo et al. (1999) suggested that the Na is from a blend of sources, 15% uniform micrometeoroid impact over the surface and the remainder (85%) from photon-induced desorption. More recently, Wilson et al. (2006) suggested that Na in the Moon's exosphere from more ubiquitous sources, such as solar and micrometeoroid bombardment, is augmented by plasma impact from the solar wind and Earth's magnetotail. These processes may also dominate at Mercury.

5 Solar Wind and Magnetospheric Interactions

Regardless of the relative roles of the processes listed in Table 2 the interactions among the solar wind, Mercury's magnetosphere, and Mercury's surface all have a strong influence on the production, maintenance, and character of Mercury's exosphere. In order to understand the generation and processes that maintain Mercury's exosphere, an understanding of the solar wind properties at Mercury and how the solar wind interacts with the planet's magnetosphere and surface is required.

As the solar wind approaches the planet, it first encounters the bow shock: the transition between the supersonic flow of interplanetary space to the subsonic, slower flows of the magnetosphere. The flow is held off by the magnetic field of the planet, but this field is not an impassable barrier. The dynamic pressure of the solar wind plasma compresses the planetary field and is balanced by the resulting magnetic pressure on the other side of the magnetopause. If the upstream dynamic pressure is sufficiently high, the magnetopause can come within a proton gyroradius of the surface, allowing direct precipitation to the surface (Goldstein et al. 1981; Kabin et al. 2000). As the IMF comes into contact with the planetary field, reconnection can occur—solar field lines join with the planetary lines (assuming an anti-parallel field configuration), and the resulting new line is dragged tailward by the solar wind. Once in the tail, another reconnection event recloses the field line with its conjugate in the opposing hemisphere. These reconnection events have several repercussions. First, they result in the peeling away of magnetic flux from the dayside of the planet, bringing the magnetopause closer to the subsolar point on the planet's surface (Slavin and Holzer 1979). Second, these events can open the magnetic cusp regions to

the inflow of solar wind plasma, allowing its interaction with the regolith along open field lines. Reconnection can also accelerate impinging charged particles, leading to enhanced sputtering or scouring of the regolith. Reconnection during the passage of a strong coronal mass ejection (CME) or magnetic cloud can literally rip away the planetary magnetic field, giving the solar wind full access to the surface (Koehn 2002). If a solar energetic particle event accompanies the CME, these energetic particles increase the sputtering effect (Leblanc et al. 2003). The only information available on Mercury's magnetosphere comes from the Mariner 10 measurements of the magnetic field (Ness et al. 1974; Simpson et al. 1974) and of the thermal plasma environment (Ogilvie et al. 1977). The thermal plasma observations provide estimates of the standoff distances of the bow shock and magnetopause consistent with the estimates based on the magnetometer measurements (Ness et al. 1975; Ogilvie et al. 1977). Any refinements in our understanding of Mercury's magnetic field come from various modeling and simulation efforts. These models and simulations are constrained by the Mariner 10 magnetic field and plasma observations, by their predictions for the generation and maintenance of the exosphere, and how these predictions for the exosphere compare with observations (specifically the neutral Na measurements). An in-depth and focused discussion of Mercury's space environment and magnetosphere is provided in a companion paper (Slavin et al. 2007), but this section provides a generalized overview as it pertains to the generation and maintenance of Mercury's exosphere.

Models of Mercury's magnetic field, its interactions with the solar wind and IMF, and the resulting possible interactions with the surface can be grouped into four basic categories: analytic models (Luhmann et al. 1998; Sarantos et al. 2001; Delcourt et al. 2002, 2003), semi-empirical models (Luhmann et al. 1998; Massetti et al. 2003), a quasi-neutral hybrid (QNH) model (Kallio and Janhunen 2003a, 2004a, 2004b), and magnetohydrodynamic (MHD) models (Kabin et al. 2000; Ip and Kopp 2002). Each model is an attempt to describe the behavior of the magnetosphere as it interacts with the passing solar wind and IMF. Of interest are the relative openness of the magnetosphere, how the solar wind and IMF orientation drive this effect, and how the solar wind gains access to the planetary surface. Calculations of the standoff distance of the magnetopause are important, as the direct collision of the solar wind with the planetary regolith affects the composition of the exosphere. Qualitatively, the predictions of these models all agree. Since Mercury's magnetic field is small and the exosphere is tenuous, solar wind ions can collide with the planet's surface along open field lines. The region of open field lines, or "cusp," varies in response to changes in, and the orientation of, the IMF. The models diverge in their predictions of the extent of the cusp region and the amount of plasma interacting with the surface on open and along closed field lines. And, of course, it is the size of the cusp region and the plasma flux that are correlated to the amount of material observed within the exosphere.

An early attempt to model the magnetosphere of Mercury was made by Siscoe and Christopher (1975). They modeled the standoff distance of the magnetopause as a function of solar wind dynamic pressure, including the effects of the distance of the planet from the Sun. They estimated that the magnetopause would be compressed to the surface of the planet less than 1% of the time. Slavin and Holzer (1979) improved this model by including the effects of magnetic flux erosion in their calculations, allowing dayside reconnection to enhance the planetward motion of the magnetopause subsolar point. They demonstrated that the standoff distance is highly variable and predicted an upper bound on the subsolar standoff distance consistent with the Mariner 10 findings. Sarantos et al. (2001) used a modified Toffoletto-Hill model (Toffoletto and Hill 1993) to characterize the behavior of the magnetosphere and open field lines as functions of the IMF. They found that a strong B_X (radial component of the IMF), much more important at Mercury than at the Earth, controls the

north–south asymmetry of the magnetosphere: for a southward IMF, a strong “positive” B_X (sunward) results in precipitation primarily in the southern hemisphere, and vice versa for a “negative” (antisunward) B_X . For a negative value of B_X , a turning B_Z regulates the size and latitude of the cusps. A strong negative B_Z drives the cusps equatorward and increases the open areas mapped by the cusps. B_Y controls the dusk–dawn asymmetry of the cusps, with a positive B_Y driving the open regions duskward, and negative B_Y producing a dawnward open region. Killen et al. (2001) used the same model to explore the effects of space weather on Mercury and to demonstrate the contribution of magnetospheric effects to the sodium variability seen by Potter et al. (1999).

Luhmann et al. (1998) used a scaled version of the Tsyganenko model (Tsyganenko and Stern 1996) of the Earth's magnetosphere to simulate that of Mercury. The Tsyganenko model allows only the Y- and Z-components of the IMF to be variables and has limited applicability to Mercury since B_X dominates there. This model predicted a very “open” magnetosphere during periods of southward IMF, which would allow the solar wind easy access to the surface. They further predicted that the relative weakness of the magnetic field of Mercury would render the magnetosphere highly sensitive to variations in the solar wind. Massetti et al. (2003) also used a modified Tsyganenko model to simulate the magnetosphere of Mercury. This model was explicitly used to map plasma precipitation onto the surface of the planet along magnetically open regions of the magnetosphere. They found that the cusps tend to map to a region ranging from 45° to 65° in latitude, with a longitudinal extent and position based on B_Y , as expected and shown in Sarantos et al. (2001). They showed a weak dependence of the open field lines on upstream dynamic pressure. They also found that the polar regions of the planet were relatively closed, as the solar wind tended to drag field lines with polar footprints into the tail.

Kallio and Janhunen (2003a, 2003b) have modeled Mercury's magnetosphere using a Quasi Neutral Hybrid (QNH) code, and they also examined the possible variation in interactions between the solar wind and planet surface based on different configurations of the IMF and dynamic pressure. Qualitatively their results are similar to MHD models, but there are distinct differences in the magnitude of the interactions predicted. Figure 9, taken from Kallio and Janhunen (2003b), maps the particle flux of impacting protons and the open/closed magnetic field line region for the following IMF configurations: (a) northward IMF, (b) southward IMF, (c) Parker spiral IMF, and (d) a high dynamical pressure case. In each case there are notable dawn–dusk particle flux asymmetries, but a north–south asymmetry develops only in the Parker-like scenario when the IMF B_X is dominant as it is at Mercury (Kallio and Janhunen 2003b). Three separate high-impact regions are apparent: (1) an “auroral” impact region equatorward of the open/closed field-line boundary, (2) a “cusp” impact region associated with the dayside noon–midnight meridian plane, and (3) a subsolar impact region apparent with high solar wind dynamical pressure. Kallio and Janhunen's (2003b) QNH model results predict that a southward IMF orientation produces a larger open field-line region than a northward IMF orientation. In addition, they predict that any north–south asymmetry in Mercury's magnetic field caused by the radial component of the IMF will also produce an asymmetry in the solar wind ion impact region on the surface, such that there will be a higher particle flux on the hemisphere that is magnetically connected to the solar wind.

MHD-based models include the acceleration effects of magnetic reconnection at Mercury, which is well-suited for studying the impact of solar-wind scouring of the regolith. Initial MHD-modeling by Kabin et al. (2000) looked at solar wind conditions with a Parker spiral IMF and showed that the magnetosphere was highly susceptible to the driving force of the solar wind. They found that the magnetic field lines for Mercury were closed at latitudes equatorward of 50° and that contact between the surface and magnetopause occurred

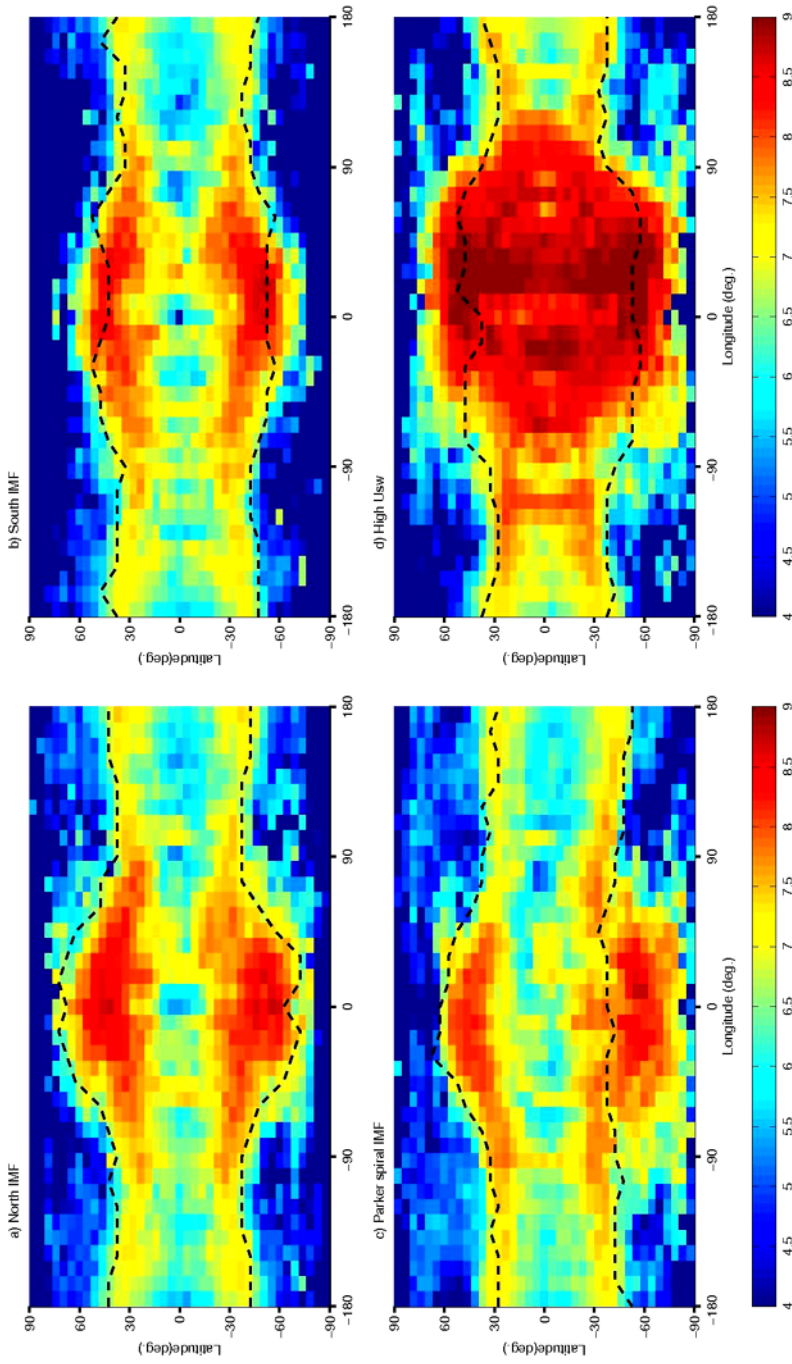


Fig. 9 Maps of the particle flux ($\text{cm}^{-2} \text{s}^{-1}$) of impacting H^+ ions and the open/closed magnetic field line region for (a) a pure northward IMF, (b) a pure southward IMF, (c) a Parker spiral IMF, and (d) a high solar wind event (Usw) (Kallio and Janhunen 2003b). The subsolar point is at the center of the image, and the *dashed lines* show the open/closed field line boundaries. The longitudes 0° and 180° correspond to local times of 0:00 and 12:00, respectively

at the subsolar point only when dynamic pressures increased by a factor of nine over the nominal conditions. They concluded that direct interaction between the solar wind and Mercury's surface is a rare phenomenon. Koehn (2002) extended the use of Kabin's model by incorporating data from the Helios spacecraft to generate upstream solar wind conditions as input for the model. This set of solar wind data includes a passing CME or magnetic cloud at 0.3 AU. This event compressed the simulated magnetopause to the planetary surface for several hours and opened the magnetopause to latitudes equatorward of 15° . During this time period, the solar wind had relatively unimpeded access to Mercury's surface. Studies by Ip and Kopp (2002) using a similar MHD model showed that there are differences in Mercury's magnetosphere, where interactions between the solar wind and surface vary as a function of the orientation of the IMF. They demonstrated that in a northward IMF configuration, Mercury's magnetosphere adopts a closed configuration and the size of the polar cap is at a minimum. In contrast, a southward IMF configuration opens up the polar cap region to its maximum size (from the pole equatorward to 20° latitude), even though the bow shock distance from the surface remains nearly the same for both configurations (Ip and Kopp 2002). Increases in dynamic pressure, such as those associated with CMEs, also push the polar cap boundary down to very low latitudes, supporting the hypothesis that solar wind variations could induce rapid temporal changes in the exospheric Na abundances (Killen et al. 2001; Ip and Kopp 2002).

There are limitations within each of these models, including the applicability of any model of the Earth's magnetosphere to Mercury. One of the major differences between the two magnetospheres is the mechanism for closing current systems. Within the Earth this is accomplished in the ionosphere, which does not exist for Mercury. Pick-up conductance within the exosphere (Cheng et al. 1987) and a conducting surface layer (Janhunen and Kallio 2004) have been proposed as possible mechanisms for Mercury. Many analytic and data-based models (e.g., Luhmann et al. 1998; Delcourt et al. 2002, 2003; Massetti et al. 2003) do not include the radial component (B_χ), which is dominant at Mercury. MHD models (Kabin et al. 2000; Ip and Kopp 2002) also include assumptions that are invalid at Mercury, such as the existence of a thin shock boundary and the assumption of thermal equilibrium. The gyroradii of heavy ions can be as large as one planetary radius at Mercury, which contradicts the assumptions of a thin shock boundary and collective ion behavior. Mariner 10 measured a nonthermal electron distribution (Criston 1987), which further invalidates the assumption of thermal equilibrium. These models do not include the effects of induced surface currents, which will generate magnetic flux that opposes or counters efforts to change Mercury's magnetic field (Hood and Schubert 1979). Sudden jumps in solar wind pressure will therefore not be as effective as one would otherwise expect in pushing the magnetopause to the surface. The induction currents add magnetic flux to the dayside magnetosphere to oppose the compression.

These models all predict that the extent of the cusps is determined by the orientation and direction of the IMF and to a lesser extent by the dynamical pressure of the solar wind. Many of these models show that dynamical pressures associated with energetic solar events (such as CMEs) can compress the magnetopause to within a gyroradius of the surface, thus allowing solar ion interaction with the regolith. However, in order to correlate the optical emission of the exosphere with these solar wind–magnetosphere interactions, an estimate of the solar wind particle flux reaching the surface is required. Flux estimates (Massetti et al. 2003; Kallio and Janhunen 2003a; Sarantos et al. 2007) are comparable to the rates needed for PSD, implying that ion sputtering is an important but variable source for Mercury's exosphere. Killen et al. (2001) demonstrated that up to 32% of the exospheric Na content can be generated from ion sputtering along open field lines when the IMF is orientated southward, but ion-sputter yields are uncertain.

6 What's Next?

To resolve many of the outstanding issues regarding the generation, maintenance, and character of Mercury's exosphere *in situ* measurements are required, including: (1) mapping of the exospheric constituents and the variation of column density with location and time; (2) mapping of the magnetic field correlated to the solar plasma environment; (3) mapping of the plasma environment with time; and (4) mapping the elemental and mineralogical properties of the surface. Temporal and spatial correlations of these types of measurements and observations will provide a better understanding of the system that supports the existence of an exosphere.

The MESSENGER spacecraft science payload has the capability to provide these *in situ* measurements. The Mercury Atmospheric and Surface Composition Spectrometer (MASCS) (McClintock and Lankton 2007) will measure and map constituents within the atmosphere with its ultraviolet-visible spectrometer while also mapping the mineral spectral properties of the surface with its visible-infrared spectrograph. The MESSENGER Magnetometer (Anderson et al. 2007) will map the magnetic field, while the Energetic Particle and Plasma Spectrometer (EPPS) (Andrews et al. 2007) will observe and map the particle and plasma environment about Mercury. The X-Ray Spectrometer (XRS) (Schlemm et al. 2007) and the Gamma-Ray and Neutron Spectrometer (GRNS) (Goldsten et al. 2007) will map the surface elemental abundances. Collectively the measurements from this suite of instruments will go a long way toward resolving many of the unknown attributes of Mercury's exosphere and related processes.

MASCS, the key instrument targeted to study the exosphere, will provide pivotal data for investigating the neutral exosphere. It will use the standard limb-scanning technique employed by Mariner 10 (Hunten et al. 1988) to measure altitude profiles of resonantly scattered sunlight by exospheric species. The resulting column emission rates will be inverted to yield density as a function of altitude that will have 25-km vertical resolution and ~300- to 500-km horizontal resolution. MASCS will study the spatial distribution and temporal behavior of the known atmospheric species (Na, Ca, K, O, and H) and will search for additional exospheric constituents (e.g., S, Al, Fe, Mg, and Si). Measurements of seasonal and geographic changes in composition and structure will provide important input for models to constrain the source and sink processes for the exosphere.

For example, simulations of MASCS operations show that the data collected will be able to test such hypotheses as correlations between local surface features and exospheric sources. These simulations use a dayside model that predicts integrated zenith column abundances for the ambient exosphere. The model, including an additional localized source, was used to simulate the exosphere for two cases: one for which thermal vaporization (TV) was assumed as the dominant source for the ambient exosphere and another for which photon-stimulated desorption was the dominant ambient source. In both cases, output column abundances from the model were distributed with altitude in accordance with density distributions associated with a particular source process. MASCS observational geometries were then calculated using the MESSENGER trajectory database and used to generate observed tangential column emission rates for each spacecraft orbit. These were combined with measured instrument performance to produce an "instrument observation."

Figure 10 summarizes the results of a simulated observation for which the ambient sodium densities are enhanced by a localized thermal vaporization source from the Caloris basin. Two cases are shown; one for which the primary source of the ambient atmosphere is thermal vaporization and the other for which the primary source is photon-stimulated desorption. Due to the 3/2 spin-orbit resonance of Mercury, the Caloris basin is observable by

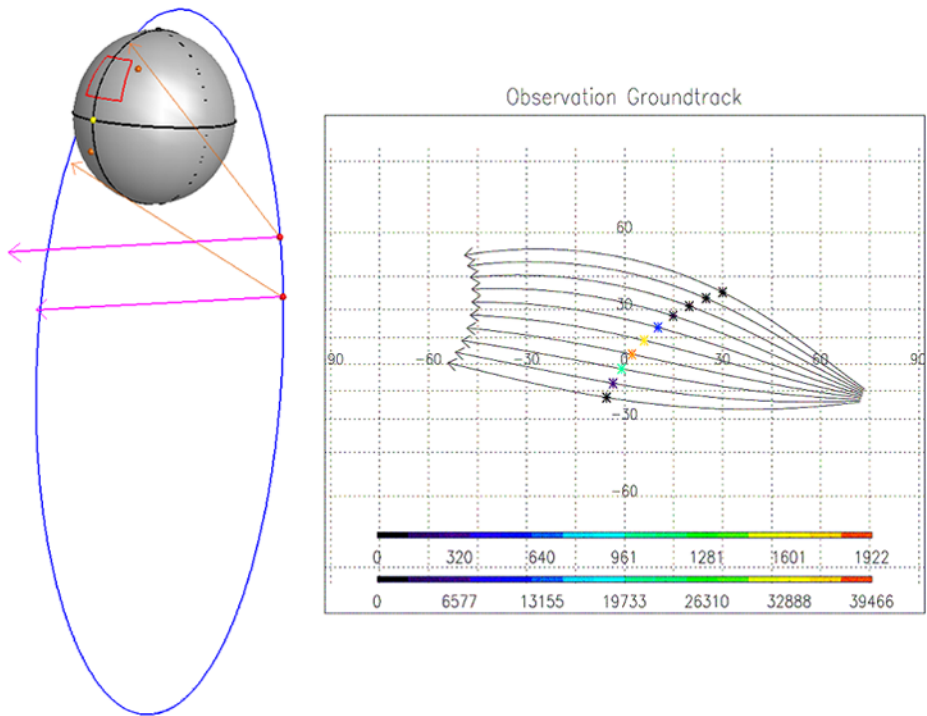


Fig. 10 (Left) Orbit of the spacecraft during the observation of the Caloris basin (red box). The orange arrows denote the line of sight at the beginning and end of the observation, while the magenta arrows denote the direction of the Sun. (Right) Ground track with the arrows denoting the line of sight. The stars represent the tangent points of the lines of sight and are color-coded to represent the instrument signal enhancement observed by MASCS above the ambient atmosphere for TV and PSD (upper and lower color bars, respectively)

MASCS only over a limited range of planet true anomaly values and also only for every other Mercury year. Observational opportunities for pointing MASCS above the region of the Caloris basin have been determined by using the MESSENGER trajectory database. The results presented in Figure 10 are for a 21-minute observation when the planet true anomaly is near 23° . During the observation the spacecraft is rotated 18.5° about the spacecraft–Sun vector, resulting in a scan that encompasses the Caloris basin and regions extending into the southern hemisphere. Note that surface temperature effects and observing geometry skew the peak emission away from the center of the enhanced region toward the subsolar point.

For these two cases, typical ambient zenith column abundances near Mercury true anomaly (TA) $\sim 23^\circ$ in the model are $2.8 \times 10^9 \text{ Na cm}^{-2}$ with a 720 K characteristic temperature and $4.35 \times 10^{11} \text{ Na cm}^{-2}$ with a 1,200 K characteristic temperature for thermal vaporization (TV) and PSD, respectively. Thus, the first case may be considered a low-energy, low-density ambient exosphere and the second considered a higher-energy, higher-density ambient exosphere. This simulation assumes that the minimum detectable column for a Caloris basin enhancement produces an instrument signal 10% above that from the ambient atmosphere signal, requiring $\sim 5 \times 10^{10} \text{ Na cm}^{-2}$ and $7.6 \times 10^{11} \text{ Na cm}^{-2}$ for TV- and PSD-generated exospheres, respectively. These values can be compared with a column of $8.0 \times 10^{11} \text{ Na cm}^{-2}$ above a southern latitude radar-bright spot reported by Sprague et

al. (1998). Repeat observations on successive orbits will reduce the minimum detectable column by a factor of 2 to 5.

7 Summary

Observations to date have demonstrated that Mercury's exosphere is highly variable and that this variability is a complicated function of location relative to the surface, Mercury true anomaly, time of Mercury day, and solar activity. Current modeling shows that the interactions among the exosphere, surface, magnetosphere, and space environment are complex. Our knowledge of these interrelated components is limited to snapshots in time, mostly constrained by the in situ observations of Mariner 10 or Earth-based telescopic observations. These data are insufficient to define fully the nature of Mercury's exosphere and provide only moderate constraints on models proposed for exosphere formation and maintenance. Neither the relative source strengths for exospheric components nor the partitioning among various release mechanisms are definitively established by the current data sets and models. One of the scientific goals for MESSENGER is to acquire an exospheric data set as a function of location relative to the surface, Mercury true anomaly, time of Mercury day, and solar activity of sufficient duration and resolution to distinguish among exospheric models and bound the relative source strengths and release mechanisms.

Many of the models and interpretations of the exospheric source and sink processes are based on assumptions regarding surface composition. What is known about the mineralogical and elemental composition of Mercury's surface is limited, however, to color data obtained by Mariner 10 (for less than half the planet) and ground-based telescopic observations (with low spatial resolution and filtered by the Earth's atmosphere). With the mineralogical and elemental compositional information to be returned by MESSENGER (Boynton et al. 2007; Head et al. 2007), additional constraints on exospheric processes and models will be possible. Equally limited is our knowledge of the magnetosphere and how it interacts with the solar environment. Measurements of Mercury's magnetic field to date are restricted to two comparatively high-altitude flybys of the planet by Mariner 10 (Slavin et al. 2007). MESSENGER will fly by the planet at low equatorial latitudes and through the magnetotail three times prior to orbit insertion. MESSENGER's orbit about Mercury will be highly elliptical, providing low-altitude information at high latitudes and multiple magnetospheric boundary crossings. All of this information will provide much-needed new constraints on the formation and maintenance mechanisms for Mercury's exosphere.

Acknowledgements The MESSENGER mission is supported by the NASA Discovery Program under contract NAS5-97271 to The Johns Hopkins University Applied Physics Laboratory. We thank Esa Kallio, Francois Leblanc, Andrew Potter, and Helmod Schleicher for the use of their figures. We thank Andrew Potter, Sean Solomon, and an anonymous reviewer for their insight and comments.

References

- G.B. Andrews et al., *Space Sci. Rev.* (2007, this issue). doi:[10.1007/s11214-007-9272-5](https://doi.org/10.1007/s11214-007-9272-5)
- B.J. Anderson et al., *Space Sci. Rev.* (2007, this issue). doi:[10.1007/s11214-007-9246-7](https://doi.org/10.1007/s11214-007-9246-7)
- F. Aumayr, H. Winter, *Phil. Trans. R. Soc. Lond. A* **362**, 77–102 (2004)
- T.A. Bida, R.M. Killen, T.H. Morgan, *Nature* **404**, 159–161 (2000)
- W.V. Boynton et al., *Space Sci. Rev.* (2007, this issue). doi:[10.1007/s11214-007-9258-3](https://doi.org/10.1007/s11214-007-9258-3)
- A.L. Broadfoot, D.E. Shemansky, S. Kumar, *Geophys. Res. Lett.* **3**, 577–580 (1976)
- B.J. Butler, D.O. Muhleman, M.A. Slade, *J. Geophys. Res.* **98**, 15003–15023 (1993)

- J.W. Chamberlain, *Planet. Space Sci.* **11**, 901–960 (1963)
- A.F. Cheng, R.E. Johnson, S.M. Krimigis, L.J. Lanzerotti, *Icarus* **7**, 430–440 (1987)
- M.J. Cintala, *J. Geophys. Res.* **97**, 947–973 (1992)
- J.E.P. Connerney, N.F. Ness, in *Mercury*, ed. by F. Vilas, C.R. Chapman, M.S. Matthews (University of Arizona Press, Tucson, 1988), pp. 494–513
- D. Crider, R.M. Killen, *Geophys. Res. Lett.* **32**, L12201 (2005). doi:[10.1029/2005GL022689](https://doi.org/10.1029/2005GL022689)
- S.P. Criston, *Icarus* **71**, 448–471 (1987)
- D.C. Delcourt, T.E. Moore, S. Orsini, A. Millilo, J.-A. Sauvaud, *Geophys. Res. Lett.* **29**, 1591 (2002). doi:[10.1029/2001GL073829](https://doi.org/10.1029/2001GL073829)
- D.C. Delcourt et al., *Ann. Geophysicae* **21**, 1723–1736 (2003)
- R.C. Elphic, H.O. Funsten III, R.L. Hervig, *Lunar Planet. Sci.* **24**, 439 (1993)
- U. Fink, H.P. Larson, R.F. Poppen, *Astrophys. J.* **287**, 407–415 (1974)
- B.E. Goldstein, S.T. Suess, R.J. Walker, *J. Geophys. Res.* **86**, 5485–5489 (1981)
- J.O. Goldsten et al., *Space Sci. Rev.* (2007, this issue). doi:[10.1007/s11214-007-9262-7](https://doi.org/10.1007/s11214-007-9262-7)
- R. Grard, *Planet. Space Sci.* **45**, 67–72 (1997)
- J.K. Harmon, *Adv. Space Res.* **19**, 1487–1496 (1997)
- J.K. Harmon, M.A. Slade, *Science* **258**, 640–642 (1992)
- R.E. Hartle, G.E. Thomas, *J. Geophys. Res.* **79**, 1519–1525 (1974)
- R.E. Hartle, K.W. Ogilvie, C.S. Wu, *Planet. Space Sci.* **21**, 2181–2191 (1973)
- J.W. Head et al., *Space Sci. Rev.* (2007, this issue). doi:[10.1007/s11214-007-9263-6](https://doi.org/10.1007/s11214-007-9263-6)
- G. Heiken, D. Vaniman, B.M. French, *Lunar Sourcebook: A User's Guide to the Moon* (Cambridge University Press, New York, 1991), 753 pp
- R.R. Hodges Jr., *J. Geophys. Res.* **78**, 8055–8064 (1973)
- L. Hood, G. Schubert, *J. Geophys. Res.* **84**, 2641–2647 (1979)
- D.M. Hunten, A.L. Sprague, *Adv. Space Res.* **19**, 1551–1560 (1997)
- D.M. Hunten, A.L. Sprague, *Meteorit. Planet. Sci.* **37**, 1191–1195 (2002)
- D. Hunten, T.H. Morgan, D.E. Shemansky, in *Mercury*, ed. by F. Vilas, C.R. Chapman, M.S. Matthews (University of Arizona Press, Tucson, 1988), pp. 562–612
- W.-H. Ip, *Geophys. Res. Lett.* **13**, 423–426 (1986)
- W.-H. Ip, *Astrophys. J.* **418**, 451–456 (1993)
- W.-H. Ip, A. Kopp, *J. Geophys. Res.* **107**, 1348 (2002). doi:[10.1029/2001JA009171](https://doi.org/10.1029/2001JA009171)
- W.-H. Ip, A. Kopp, *Adv. Space Res.* **33**, 2172–2175 (2004)
- P. Janhunen, E. Kallio, *Ann. Geophysicae* **22**, 1829–1837 (2004)
- R.E. Johnson, in *Atmospheres in the Solar System: Comparative Aeronomy*, ed. by M. Mendillo, A. Nagy, J.H. Waite. Geophysical Monograph, vol. 130 (American Geophysical Union, Washington, 2002), pp. 203–219
- K. Kabin, T.I. Gombosi, D.L. DeZeeuw, K.G. Powell, *Icarus* **143**, 397–406 (2000)
- T. Kadono, A. Fujiwara, *J. Geophys. Res.* **101**, 26097–26110 (1996)
- T. Kadono et al., *Geophys. Res. Lett.* **29**, 1979 (2002). doi:[10.1029/2002GL015694](https://doi.org/10.1029/2002GL015694)
- E. Kallio, P. Janhunen, *Ann. Geophysicae* **21**, 2133–2145 (2003a)
- E. Kallio, P. Janhunen, *Geophys. Res. Lett.* **30**, 1877 (2003b). doi:[10.1029/2003GL017842](https://doi.org/10.1029/2003GL017842)
- E. Kallio, P. Janhunen, *Eos Trans. Am. Geophys. Union* **85** (Fall meeting suppl.) (2004a), abstract P23A0241K
- E. Kallio, P. Janhunen, *Adv. Space Res.* **33**, 2176–2181 (2004b)
- R.M. Killen, *Geophys. Res. Lett.* **16**, 171–174 (1989)
- R.M. Killen, D. Crider, *Eos Trans. Am. Geophys. Union* **85** (Fall meeting suppl.) (2004), abstract P23A-0248
- R.M. Killen, A.E. Potter, T.H. Morgan, *Icarus* **85**, 145–167 (1990)
- R.M. Killen, J. Benkhoff, T.H. Morgan, *Icarus* **125**, 195–211 (1997)
- R.M. Killen, A.E. Potter, A. Fitzsimmons, T.H. Morgan, *Planet. Space Sci.* **47**, 1449–1458 (1999)
- R.M. Killen et al., *J. Geophys. Res.* **106**, 20509–20525 (2001)
- R.M. Killen, M. Sarantos, A.E. Potter, P. Reiff, *Icarus* **171**, 1–19 (2004a)
- R.M. Killen, M. Sarantos, P. Reiff, *Adv. Space Res.* **33**, 1899–1904 (2004b)
- R.M. Killen, T.A. Bida, T.H. Morgan, *Icarus* **173**, 300–311 (2005)
- P.L. Koehn, Ph.D. thesis, University of Michigan, Ann Arbor, 2002, 183 pp
- P.L. Koehn, A.L. Sprague, *Planet. Space Sci.* **55**, 1530–1540 (2007)
- P.L. Koehn, T.H. Zurbuchen, G. Gloeckler, R.A. Lundgren, L.A. Fisk, *Meteorit. Planet. Sci.* **37**, 1173–1190 (2002)
- S. Kumar, *Icarus* **28**, 579–591 (1976)
- H. Lammer et al., *Icarus* **166**, 238–247 (2003)
- F. Leblanc, R.E. Johnson, *Icarus* **164**, 261–281 (2003)
- F. Leblanc, J.G. Luhmann, R.E. Johnson, M. Liu, *Planet. Space Sci.* **51**, 339–352 (2003)

- J.G. Luhmann, C.T. Russell, N.A. Tsyganenko, *J. Geophys. Res.* **103**, 9113–9119 (1998)
- T.E. Madey, B.V. Yakshinskiy, V.N. Ageev, R.E. Johnson, *J. Geophys. Res.* **103**, 5873–5887 (1998)
- V. Mangano et al., *Planet. Space Sci.* **55**, 1541–1556 (2007)
- T.E. Madey, R.E. Johnson, T.M. Orlando, *Surf. Sci.* **500**, 838–858 (2002)
- S. Marchi, A. Morbidelli, G. Cremonese, *Astron. Astrophys.* **431**, 1123–1127 (2005)
- S. Massetti et al., *Icarus* **166**, 229–237 (2003)
- W.E. McClintock, M.R. Lankton, *Space Sci. Rev.* (2007, this issue). doi:[10.1007/s11214-007-9264-5](https://doi.org/10.1007/s11214-007-9264-5)
- M.A. McGrath, R.E. Johnson, L.J. Lanzerotti, *Nature* **323**, 694–696 (1986)
- M. Mendillo, J. Baumgardner, *Nature* **377**, 404–406 (1995)
- M. Mendillo, J. Baumgardner, J. Wilson, *Icarus* **137**, 13–23 (1999)
- T.H. Morgan, H.A. Zook, A.E. Potter, *Icarus* **75**, 156–170 (1988)
- N.F. Ness, K.W. Behannon, R.P. Lepping, Y.C. Whang, K.H. Schatten, *Science* **185**, 151–160 (1974)
- N.F. Ness, K.W. Behannon, R.P. Lepping, Y.C. Whang, K.H. Schatten, *J. Geophys. Res.* **80**, 2708–2716 (1975)
- K.W. Ogilvie, J.D. Scudder, V.M. Vasyliunas, R.E. Hartle, G.L. Siscoe, *J. Geophys. Res.* **82**, 1807–1824 (1977)
- A.E. Potter, *Geophys. Res. Lett.* **22**, 3289–3292 (1995)
- A.E. Potter, T.H. Morgan, *Science* **229**, 651–653 (1985)
- A.E. Potter, T.H. Morgan, *Icarus* **67**, 336–340 (1986)
- A.E. Potter, T.H. Morgan, *Science* **248**, 835–838 (1990)
- A.E. Potter, T.H. Morgan, *Planet. Space Sci.* **45**, 95–100 (1997)
- A.E. Potter, R.M. Killen, T.H. Morgan, *Planet. Space Sci.* **47**, 1141–1148 (1999)
- A.E. Potter, R.M. Killen, T.H. Morgan, *J. Geophys. Res.* **105**, 15073–15084 (2000)
- A.E. Potter, C.M. Anderson, R.M. Killen, T.H. Morgan, *J. Geophys. Res.* **107**, 5040 (2002a). doi:[10.1029/2000JE001493](https://doi.org/10.1029/2000JE001493)
- A.E. Potter, R.M. Killen, T.H. Morgan, *Meteorit. Planet. Sci.* **37**, 1165–1172 (2002b)
- A.E. Potter, R.M. Killen, M. Sarantos, *Icarus* **181**, 1–12 (2006)
- M.S. Robinson, P.G. Lucey, *Science* **275**, 197–198 (1997)
- M. Sarantos, Ph.D. dissertation, Rice University, Houston, TX, 2005, 81 pp
- M. Sarantos, P.H. Reiff, T.W. Hill, R.M. Killen, A.L. Urquhart, *Planet. Space Sci.* **49**, 1629–1635 (2001)
- M. Sarantos, R.M. Killen, D. Kim, *Planet. Space Sci.* (2007). doi:[10.1016/j.pss.2006.10.011](https://doi.org/10.1016/j.pss.2006.10.011)
- H. Schleicher, G. Wiedemann, H. Wohl, T. Berkefeld, D. Soltau, *Astron. Astrophys.* **425**, 1119–1124 (2004)
- C.E. Schlemm II et al., *Space Sci. Rev.* (2007, this issue). doi:[10.1007/s11214-007-9248-5](https://doi.org/10.1007/s11214-007-9248-5)
- D.E. Shemansky, in *AIP Conf. Proc.* **63**, *Rarefied Gas Dynamics 23rd Int. Symp.*, ed. by A.D. Ketsdever, E.P. Muntz, Chap. 9, Topics in Astrophysics (2003), pp. 687–695
- D.E. Shemansky, A.L. Broadfoot, *Rev. Geophys. Space Phys.* **15**, 491–499 (1977)
- C.-Y. Shih, L.E. Nyquist, D.D. Bogard, E.J. Dasch, B.M. Bansal, H. Wiesman, *Geochim. Cosmochim. Acta* **51**, 3255–3271 (1987)
- J.A. Simpson, J.H. Eraker, J.E. Lamport, P.H. Walpole, *Science* **185**, 160–166 (1974)
- G. Siscoe, L. Christopher, *Geophys. Res. Lett.* **2**, 158–160 (1975)
- M.A. Slade, B.J. Butler, D.O. Muhleman, *Science* **258**, 635–640 (1992)
- J.A. Slavin, R.E. Holzer, *J. Geophys. Res.* **84**, 2076–2082 (1979)
- J.A. Slavin et al., *Space Sci. Rev.* (2007, this issue). doi:[10.1007/s11214-007-9154-x](https://doi.org/10.1007/s11214-007-9154-x)
- W.H. Smyth, M.L. Marconi, *Astrophys. J.* **441**, 839–864 (1995)
- A.L. Sprague, *Icarus* **84**, 93–105 (1990)
- A.L. Sprague, *J. Geophys. Res.* **97**, 18257–18264 (1992)
- A.L. Sprague, R.W. Kozlowski, D.M. Hunten, *Science* **129**, 506–527 (1990)
- A.L. Sprague, D.M. Hunten, K. Lodders, *Icarus* **118**, 211–215 (1995)
- A.L. Sprague, D.M. Hunten, F.A. Grosse, *Icarus* **123**, 345–349 (1996)
- A.L. Sprague et al., *Icarus* **129**, 506–527 (1997)
- A.L. Sprague, W.J. Schmitt, R.E. Hill, *Icarus* **136**, 60–68 (1998)
- R.G. Strom, A.L. Sprague, *Exploring Mercury: The Iron Planet* (Springer, New York, 2003), 216 pp
- T.J. Stubbs, R.R. Vondrak, W.M. Farrell, *Lunar Planet. Sci.* **36** (2005), abstract 1899
- S. Sugita, K. Hamano, T. Kadono, P.H. Schultz, T. Matsui, in *Impact Cratering: Bridging the Gap between Modeling and Observations* (Lunar and Planetary Institute, Houston, 2003), p. 68
- F.R. Toffoletto, T.W. Hill, *J. Geophys. Res.* **98**, 1339–1344 (1993)
- N.A. Tsyganenko, D.P. Stern, *J. Geophys. Res.* **101**, 27187–27198 (1996)
- A.L. Tyler, R.W. Kozlowski, L.A. Lebofsky, *Geophys. Res. Lett.* **15**, 808–811 (1988)
- R.R. Vondrak, T.J. Stubbs, W.M. Farrell, *Eos Trans. Am. Geophys. Union* **85** (Fall meeting suppl.) (2004), abstract SM53A0401
- J. Wilson, M. Mendillo, H.E. Spence, *J. Geophys. Res.* **111**, A07207 (2006). doi:[10.1029/2005JA011364](https://doi.org/10.1029/2005JA011364)
- B.V. Yakshinskiy, T.E. Madey, *Nature* **400**, 642–644 (1999)
- B.V. Yakshinskiy, T.E. Madey, V.N. Ageev, *Surf. Rev. Lett.* **7**, 75–87 (2000)
- N. Yan, F. Leblanc, E. Chassefiere, *Icarus* **181**, 348–362 (2006)